PAPER

X-ray spectroscopy as a probe for lithium polysulfide radicals

Tod A. Pascal,* C. D. Pemmaraju and David Prendergast*

The discharge mechanism in lithium sulfur batteries is still unknown and has been purported to involve significant concentrations of polysulfide radicals. Methods capable of quantifying these species in solution are therefore of paramount importance to revealing electrochemical pathways. Here we utilize DFT based X-ray Absorption Spectroscopy (XAS) simulations at the sulfur K-edge to obtain the spectra of polysulfide molecules in neutral, radical (−1) and dianionic (−2) charge states. Our calculations indicate that, contrary to recent propositions, the observed low energy, pre-edge feature in S K-edge XAS near 2470 eV is not exclusively due to radical species, but rather arises predominantly from core-excitations of terminal atoms, at the ends of linear polysulfides, to σ^* orbitals, consistent with our previous results for the dianionic species. We do however find a spectral feature unique to radicals, lying 0.5–1 eV below the established pre-edge, that arises from $1s \rightarrow \pi^*$ transitions of the terminal atoms. Existing measurements on polysulfides show no evidence for such transitions. We predict that detection of linear radicals in polysulfide mixtures using XAS is limited to high mole fractions ($>20\%$), due to the relatively weak XAS intensity of this π^* feature.

1. Introduction

Sulfur is the tenth most abundant element in the earth's crust[1] and exhibits a great degree of electronic versatility by accepting oxidation states ranging from +6 to −2.[2,3] At ambient conditions, it readily reacts to form various salts and minerals, but also exists in its purely elemental form as rings of S atoms, ranging in size from 6 to 20.[4] Of the many ring structures, the alpha phase of octasulfur (α-S_8) is the most stable at ambient conditions.[5]

The chemical reactivity, low mass density, large availability and diversity of sulfur containing compounds makes sulfur particularly attractive in materials chemistry, and recently, as a component of rechargeable lithium–sulfur (Li–S) batteries. Li–S batteries are one of the more promising technologies being investigated for advanced renewable energy storage, and have five times the theoretical energy density of lithium ion batteries, and one-fifth that of gasoline.[6] The success of this technology ultimately hinges on revealing the fundamental mechanisms underlying its electrochemistry and thereby overcoming its most significant drawback: rapid capacity fading during cycling,[7–9] leading eventually to battery failure.

Understanding the failure mechanism in turn depends on an ability to characterize the products and reaction intermediates during different stages of electrochemical cycling. However, despite

The Molecular Foundry, Lawrence Berkeley National Laboratory, Berkeley, CA 94720, USA. E-mail: tod.a.cp@gmail.com, dgprendergast@lbl.gov

much effort over the last five years, we still lack consensus on the stepwise electrochemical mechanisms involved in conversion of sulfur to lithium sulfide and back again,[10] due in no small part to the inherent difficulties in performing *in situ* experiments. Additionally, it is likely that a rich family of chemical species in Li–S cathodes and electrolytes exist in thermodynamic equilibrium, with inter-conversion to initially non-equilibrium distributions being driven by voltage.

To this end, several recent experimental studies have used spectroscopic techniques to probe the solution phase chemistries in Li–S batteries.[11–15] One class of studies have employed X-ray absorption spectroscopy (XAS),[11,15–19] the process whereby a core electron is excited to available empty electronic states upon the absorption of a resonant X-ray photon. XAS is attractive since it provides element-specific information by tuning photons to a specific absorption onset (edge), and the spectral fine structure at this absorption edge, if properly interpreted, reveals information on the charge state, bonding configuration, and chemical environment around the excited atom.

For all but the simplest molecules in the gas phase however, interpretation of X-ray spectral features is non-trivial. XAS can be predicted from *ab initio* calculations, although, for Li–S systems, there have been relatively few studies[20,21] to date, possibly due to the computational complexity of modeling solvated polysulfides. As a result, experimental measurements are usually referenced to established standards,[15,16] under the assumption that the spectral features in the standards provide a sufficient compositional or numerical basis, so that unique linear combinations of these

This journal is © the Owner Societies 2015

Phys. Chem. Chem. Phys., 2015, **17**, 7743–7753 | 7743

standards can reproduce measurements. As a point of reference, X-ray absorption of α-S_8 at the sulfur K-edge (*i.e.*, 1s → 3p excitations) is dominated by a single peak, the so-called "white line" at ∼2472–2473 eV.[22,23] Various experimental measurements have shown that S K-edge spectra of dissolved lithium polysulfides are generally characterized by a low energy absorption feature (denoted the pre-edge) between 2469 and 2471 eV, depending on the calibration, and a more prominent (main-edge) feature near 2472 eV,[15,16,24,25] coincident with the α-S_8 white line.

The fact that the pre-edge is absent in α-S_8 led many to speculate that this feature arises from different types of sulfur-containing molecules in the system. It was already known that the trisulfur radical ion ($S_3^{\bullet-}$), stabilized in tectosilicate cages to form lazurite, gives these minerals their characteristic deep blue, ultramarine color and has a pre-edge XAS feature roughly 2–3 eV below the white line.[26] Based on earlier evidence of the $S_3^{\bullet-}$ radical from complimentary spectroscopic techniques, it was then proposed that the pre-edge evident in the spectra of lithium polysulfides arises from the presence of significant concentrations of the $S_3^{\bullet-}$ radical,[16,24] and that this species plays a prominent role in electrochemical processes.

This hypothesis on the origin on the pre-edge feature in the XAS of lithium polysulfides has been challenged recently by density functional theory (DFT) calculations,[20,21] which have shown that the XAS of the dianionic polysulfides (S_x^{2-}; x = 2,...,8) are also characterized by pre-edge and main-edge features in the same energy range. Further, although polysulfide radical anions have been shown to form stable compounds with alkali metal cations in highly polar solvents such as DMF and DMSO,[27–29] it is known that these anions are unstable in low dielectric solvents, such as the ethereal solvents or polymers commonly used in Li–S batteries, and that they readily dimerize in the presence of appropriate counterions.[23,30,31] Possibly recognizing this fact, more recent experiments[11,18,25] do not invoke radicals as the origin of the pre-edge feature in the S K-edge XAS.

Methods capable of detecting and quantifying the concentration of radical species in Li–S battery materials are thus of fundamental importance to resolving this controversy and, by extension, gaining insight into the reaction mechanisms that underlie Li–S battery operation. Electron spin paramagnetic resonance (EPR or ESR) spectroscopy is the most direct method for detecting radicals, providing information about the interaction of unpaired electrons with the surrounding nuclei.[12,32] However, quantifying the relative amounts of the various possible polysulfide radicals (with respect to a background of non-radical species) remains difficult. Thus, EPR is usually combined with complementary spectroscopic techniques, mostly UV-visible absorption spectroscopy, inspired by the dramatic color differences that purportedly arise from polysulfides of different lengths. Yet here again, the assignment of the measured spectra to a particular polysulfide molecule is non-trivial and subject to some debate.[12,33]

Due to its elemental specificity and chemical sensitivity, XAS potentially offers a means to differentiate between the various charge states of lithium polysulfide species. In this contribution, we present DFT based simulations of the XAS of neutral, radical and dianionic polysulfides, ranging from disulfur to octasulfur (S_8^x). We find that, with the exception of the special case that is disulfur, the low energy pre-edge feature in S K-edge XAS results mostly from dangling (terminal) sulfur bonds irrespective of the molecular charge state, and is not solely the signature of radical species, such as $S_3^{\bullet-}$, as has been proposed.[16,24] Although the ground state electronic structure of short polysulfide radicals are characterized by a half-filled π* orbital (this orbital is filled in the dianion and thus inaccessible to X-ray excitations), our calculations predict that 1s → π* excitations would occur at energies below the typical pre-edge of polysulfide dianions. In the case of the trisulfur radical ($S_3^{\bullet-}$), these transitions should appear as a faint pre-edge feature in the XAS below near 2468.5 eV, which we predict to be detectable in XAS only for relatively large (>20%) radical concentrations in polysulfide mixtures.

2. Results

In this section, we demonstrate how molecular charge state and changes in the S–S bond geometry and partial atomic charges, brought on by finite temperature dynamics, conspire to determine the energetic position and intensity of various features in the S K-edge XAS. The objective here is to start with the smallest polysulfide molecule, disulfur (S_2), in various charge states, and demonstrate how one would expect the XAS peak positions and intensities to change, based on a simple molecular orbital (MO) analysis. Once established, we will then consider three more complex, longer chain polysulfides: trisulfur, tetrasulfur and octasulfur. We will pay particular attention to the "ubiquitous"[34] trisulfur molecule, as this species is most often postulated as being present in large quantities in working Li–S electrochemical cells.

2.1. Disulfur

2.1.1. Neutral S_2. To start, we performed a geometry optimization of the S_2 molecule in each of three charge states: neutral, radical (−1) and dianion (−2). All of our calculations were performed at the density functional theory (DFT) level within the Perdew–Burke–Ernzerhof (PBE)[35] form of the generalized-gradient approximation to the exchange–correlation energy. As a figure of merit, we found that the calculated equilibrium S–S bond length increases from 1.930 to 2.009 to 2.076 Å for the S_2 (singlet), $S_2^{\bullet-}$ and S_2^{2-} species, respectively, in rather good agreement with 1.924, 2.004 and 2.115 Å, respectively, obtained from more accurate levels of theory.[36] The increase in bond length with increasing molecular charge reflects the filling of the π* anti-bonding orbitals, which weakens the S–S bond. Of course the ground state of the neutral S_2 molecule should be a triplet $^3\Sigma_g^-$, which we calculate is 0.42 eV lower in energy than the singlet, and has an equilibrium bond length of 1.968 Å, both in general agreement with published results.[37]

The ground state (GS) electron configuration of the neutral S_2 molecule is $KKLL(\sigma_g 3s)^2(\sigma_u 3s)^2(\sigma_g 3p)^2(\pi_u 3p)^4(\pi_g 3p)^2$, where the singly occupied molecular orbital (SOMO) $(\pi_g 3p)^2$ is of π* symmetry with two unpaired spins, and the lowest unoccupied molecular orbital (LUMO) $(\sigma_u 3p)$ is of σ* symmetry.[38] Upon absorption of

resonant X-ray photons, two sets of transitions are possible in the near-edge region:

(1) a single 1s → SOMO transition resulting in a 3Π state ($\sigma\pi^3$) with 1 unpaired electron in the valence subspace and

(2) two 1s → LUMO transitions resulting in Σ^- states of either quartet ($^4\Sigma^-$, high spin) or doublet ($^2\Sigma^-$, low spin) configurations.

A previous *ab initio* multi-reference configuration interaction (MRCI) calculation has shown the quartet state to be 1.15 eV lower in energy.[39] An important difference between that study and our approach is that we don't explicitly consider the spin of the remaining 1s core electron after the XAS process, meaning that our calculated σ* states do not properly satisfy the correct spin multiplicities. Nevertheless, and consistent with the results of the MRCI study, we predict three predominant XAS peaks (Fig. 1a):

(1) two peaks associated with transitions from the minority spin channel (S^β): a low energy 1s → π* peak and another 1s → σ* transition 4.7 eV higher in energy, resulting in a doublet state;

(2) a separate 1s → σ* transition from the majority spin channel (S^α) 3.1 eV higher than the 1s → π*, resulting in a quartet state (Fig. 1b).

The previous MRCI study calculated a 2:1 ratio in the intensity of the quartet and doublet states.[39] Within the single determinant Kohn–Sham DFT approach we employ, we cannot access the full spin multiplicity of the states within the quartet

and doublet valence configurations associated to the 1s → σ* transition. The Kohn–Sham solution in each case is simply characterized by a total spin-projection $S_z = S_{max}$ ($S_{max} = 3/2$ and 1/2 for the quartet and doublet states respectively). Further, the energies and oscillator strengths of the two 1s → σ* states are obtained from Kohn–Sham eigenvalues and wavefunctions and the single particle approximation of the many-body transition matrix elements assumes a constant scaling factor.[40] Therefore the pre-factors arising from the different multiplicities of the quartet and doublet states do not appear in our method. Nevertheless, our approach reproduces the energy splitting between the quartet and doublet states and recovers some of the intensity difference by self consistently regenerating the Kohn–Sham wavefunctions and spectrum in the presence of the excited electron and core-hole, although this only results in 16% increase in the quartet relative to the doublet.

Turning now to the experimental measurement, we find that direct comparison is complicated, since the S_2 molecule is not the stable form of sulfur at ambient conditions. A high temperature (565 K) experimental spectrum has been published, obtained as the difference spectrum with respect to lower temperature measurements under the assumption that S_2 is the dominant molecular species at this higher temperature.[39] This experimental XAS spectra is characterized by two main features: a broad, low energy feature centered near 2468.95 eV that has been assigned to the S 1s → π* transitions, and another,
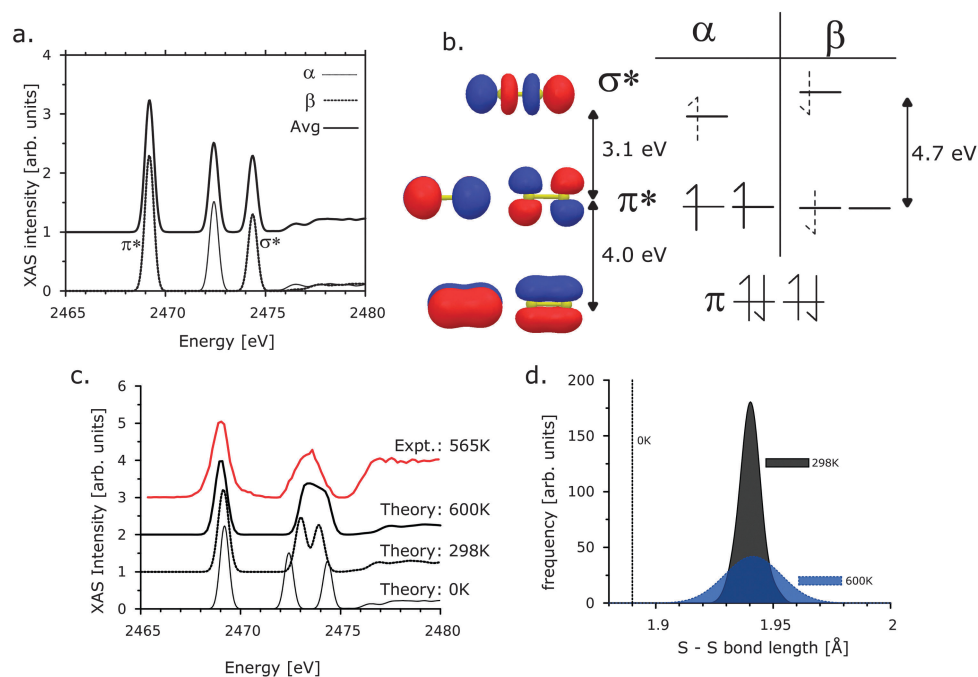
Fig. 1 (a) Calculated S K-edge XAS of S_2 (solid black line), showing contributions from the majority (S^α – dashed line) and minority (S^β – dotted line) spin channels. (b) Energy level diagram of molecular S_2 indicating possible X-ray excitations in majority or minority spin channels: electrons in ground state occupations are indicated by solid arrows; possible energy levels for the excited 1s core electron are indicated by dashed arrows. The electron density ($|\psi|^2$ sgn(ψ)) and phase of the π, π* and σ* orbitals are also shown. We adopt the convention that the positive phase of the density is colored blue while the negative phase is colored red. (c) Temperature dependence of the calculated XAS of S_2. The spectra are ensemble averages of snapshots from an AIMD simulation at the appropriate temperature. The calculated 600 K spectrum closely resembles the experiment at 565 K. Note that since our calculated oscillator strengths do not have a direct correspondence to the experimental intensities, our calculated spectra are all scaled by an arbitrary constant (7168) to match the experimental 1st peak. (d) S−S bond length distributions from AIMD simulations at 298 and 600 K.

broader feature centered near 2473.2 eV, decomposed as two separate features located at 2472.82 and 2473.57 eV and assigned to the S 1s → σ* transitions described above. As shown in Fig. 1c, our calculated spectra obtained from sampling a 600 K *ab initio* molecular dynamics (AIMD) trajectory provide a better reproduction of experiment: the formal 1.5 eV separation in the σ* peaks at 0 K is progressively reduced at higher temperatures due to S–S bond length fluctuations (Fig. 1d). Additionally, the XAS features are generally red-shifted with increasing temperature due to longer average S–S bonds; in the frontier orbitals picture, the HOMO–LUMO gap of a diatom arises from the overlap between the orbitals, which decreases as the inverse of squared bond length.

2.1.2. S_2 radical. Turning our attention now the radical $S_2^{\bullet-}$ ion, the GS SOMO has a $(\pi_g 3p)^3$ electronic configuration, with only one unpaired electron in the π* orbital. As was the case in the neutral molecule, three major transitions are allowed in the XAS (Fig. 2a): 1s → π* and 1s → σ* (singlet, no net spin) transitions from the minority spin and a 1s → σ* (triplet, high spin) from the majority spin channels so that the resulting XAS spectrum has three main features (Fig. 2b). There are some differences in the peak positions of the radical compared to the neutral molecule that warrant further examination. First, we calculate π* → σ* splittings of 1.3 (3.3) eV for the majority (minority) channel of the radical, compared to 3.1 (4.7) eV for the neutral molecule. Second, the π* and σ* peak positions in the radical are red-shifted by 0.7 and 0.5 eV respectively compared to the neutral (Fig. 3). Finally, the intensity of the 1s → π* XAS peak in the radical is decreased by ∼55%, compared to the neutral molecule.

These differences in the XAS spectra can be explained by considering four factors: (1) the longer S–S bond in the radical leads to smaller SOMO–LUMO gaps, as mentioned before; (2) the filling of one of the π* orbitals of the radical destabilizes the minority spin σ* orbital due to a reduction in exchange interactions; (3) the red-shifting of the peak positions of the radical due to the additional valence electronic screening of the S 1s core electron and associated reduction in its binding energy; and (4) decrease in the first peak intensity of the radical due to the fact that only one π* orbital is available for transition rather
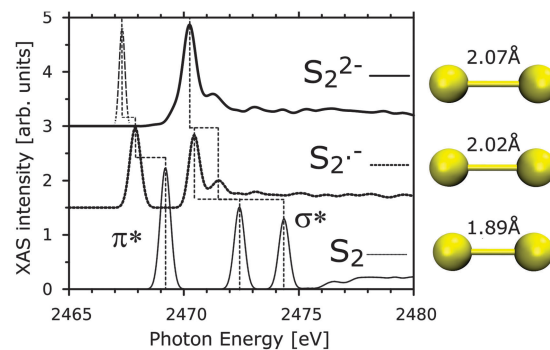

Fig. 3 Comparison of the calculated S K-edge XAS of molecular S_2, the radical $S_2^{\bullet-}$ and dianion S_2^{2-}. Dashed vertical lines are included to indicate the position of the 1s → π* and 1s → σ* transitions. For the dianion, we indicate the filled π* orbital in dashed lines.

than two, in the neutral triplet. In the case of the red-shift due to additional screening, we consider the core-excitation heuristically as a two-step process: (1) creation of the core-hole and (2) response of the valence shell to that excitation. In this picture, the presence of more valence electrons can stabilize a core-excited state relative to the ground state.

2.1.3. S_2 dianion. The process of forming the dianion S_2^{2-}, starting from the radical, involves placing an additional electron in the lowest lying empty orbital, which in this case is the π* orbital. As a result, the π* orbital is completely filled. Consequentially, the spin degeneracy of the σ* orbital is restored, and the first available transition for the excited 1s core electron is the empty σ* orbital and the resultant XAS is dominated by a single sharp feature centered near 2470.5 eV (Fig. 3). Further, the σ* peak in the dianion is red-shifted by 0.7 eV compared to the radical, again due to increased electronic screening and a slightly longer S–S bond.

2.2. Trisulfur

The trisulfur $S_3^{\bullet-}$ radical is of particular interest, due to its purported importance in many aspects of inorganic chemistry,[34] including Li–S electrochemistry, although it is best known as the origin of the characteristic deep blue color in ultramarine pigments derived from lazurite minerals, which have recently
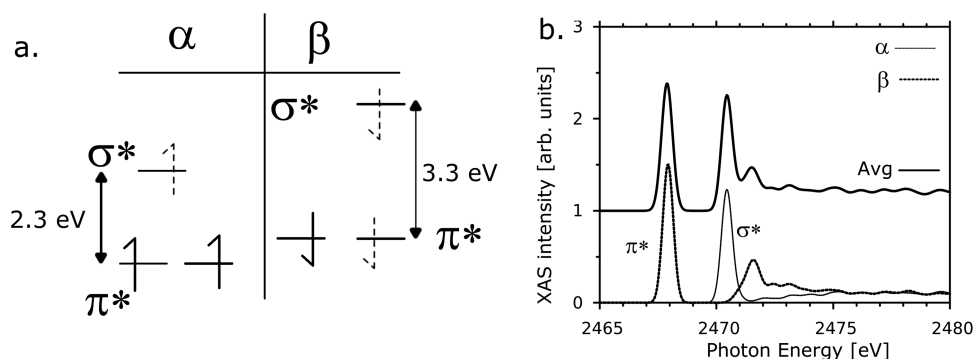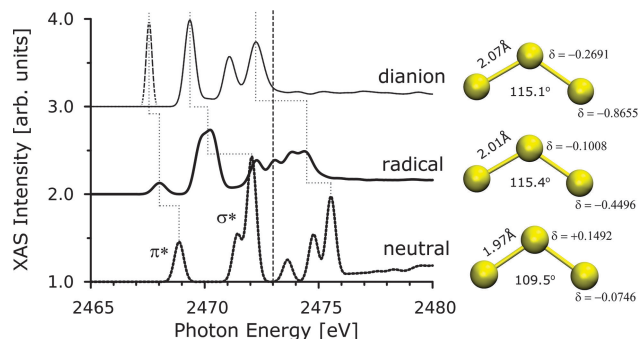

Fig. 2 (a) Energy level diagram of the $S_2^{\bullet-}$ radical ion after absorption of the X-ray photon. The π*–σ* splittings are indicated. Note the breaking of the degeneracy of the filled and half filled π* orbitals in the ground state. (b) Calculated S K-edge XAS of the $S_2^{\bullet-}$ radical ion. The line styles are the same as in Fig. 1b. The peak positions of the π* and σ* features are indicated.

7746 | *Phys. Chem. Chem. Phys.*, 2015, **17**, 7743–7753

This journal is © the Owner Societies 2015

Fig. 4 Comparison of the calculated XAS of neutral, radical and dianionic trisulfur molecules at 0 K. The optimized S–S bond length, S–S–S angle and partial atomic charges (from Bader analysis[58,59]) are indicated to the right. Broken dotted lines are added to indicate the relative positions of the π* and σ* features. The straight vertical dashed line demarcates the high energy σ* feature >2473 eV that is prominent in the radical and neutral molecules, but shifted to lower energies in the dianion due to core level shifts.

been characterized using XAS.[26,30,41] We pay special attention to the XAS of this molecule since a recent study has suggested that no other radicals species are likely to be present in the electrolyte of a Li–S battery.[20] Our DFT-PBE optimization at 0 K reveals that the ground state of $S_3^{\bullet-}$ is a $^1A_1$ doublet with C_{2v} geometry and an average S–S bond length of 2.009 Å, and a S–S–S angle of 115.5° (Fig. 4), in reasonable agreement with S–S bond lengths of 1.991–2.04 Å and S–S–S bond angles of 113.4–115.8° in the literature.[36] We also found a more closed, ring isomer structure (D_{3h} geometry) at 0 K, 0.27 eV higher in energy with an increased S–S bond length of 2.120 Å.

As shown in Fig. 4, the XAS is characterized by four features: (1) a low energy peak centered near 2468.1 eV (2) a broad, distinct peak centered near 2470.8 eV (3) a less distinct peak

near 2472.5 eV and (4) a broad collection of peaks from 2473–2476 eV. The XAS of the radical stands in contrast to that of the neutral molecules, which is characterized by additional, more distinct peaks that are generally blue shifted by ∼1 eV, and to that of the dianion, which is characterized by three well resolved peaks that are red-shifted by ∼0.75 eV. The relative shifts of the peaks in the XAS spectrum reflects changes in the core-level binding energies and occupied/unoccupied orbital splitting (due to changes in the S–S bonds), as was found for disulfur.

The calculated lineshapes and number of distinct features of our DFT-XCH XAS calculations of the trisulfur radical is in general agreement with the time dependent DFT (TD-DFT) calculations of Vijayakumar et al.[20] The TD-DFT spectrum is generally smoother likely reflecting the use of a larger Gaussian broadening parameter than ours (0.2 eV). There are some differences in the peak positions however that need to be addressed. We predict a low energy π* peak at 2468.1 eV, however the first peak in the TD-DFT study is located at ∼2472 eV. We have found that the peak position of a typical TD-DFT calculation is a dramatic function of the DFT functional used, thus any such calculation would have to be aligned to some known standard. Due to the nature of our calculations, all of our spectra are rigidly shifted by an empirical factor chosen to match the first peak position in the experimental spectrum of gaseous SF$_6$ (see details in the Methods section). Using this approach, we are able to predict the onset of a diverse array of sulfur containing compounds to within 0.1 eV of experiments and so are confident with our predictions on the peak positions of the trisulfur radical.

Analysis of the contributions to the XAS of the radical, resolved by spin, reveals that the low energy peak near 2468 eV arises solely from the two terminal sulfur atoms, and more specifically from the 1s → π* (minority spin) transitions on
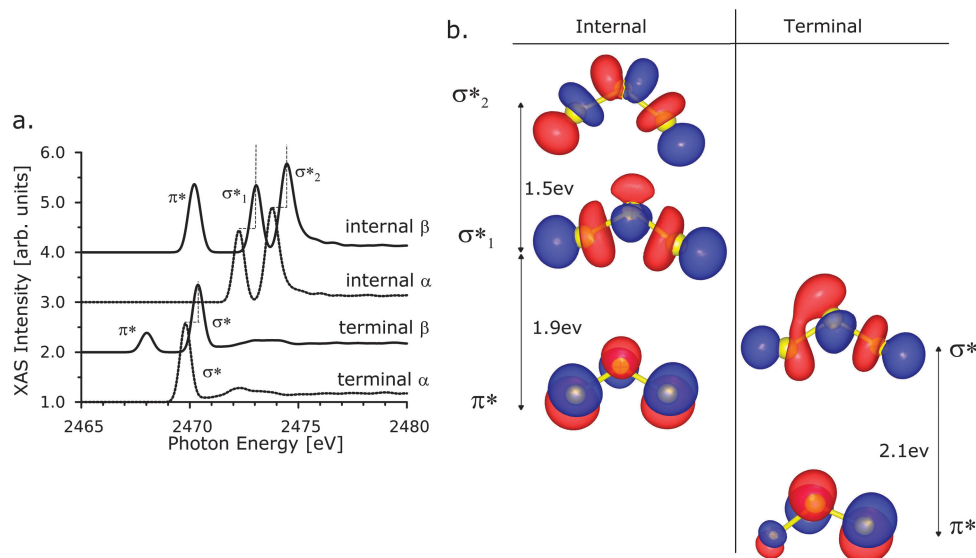
Fig. 5 (a) Calculated S K-edge XAS of the radical $S_3^{\bullet-}$ ion, separated into contributions from the central S atom and the two terminal S atoms. Additionally, the contributions of each to the XAS from the majority (α – dashed line) and minority (β – solid line) spin channels are shown. (b) Electron density of the core-excited π* and σ* orbitals in the trisulfur radical molecule at 0 K. The states resulting from excitations to the internal and terminal sulfur atoms are presented.
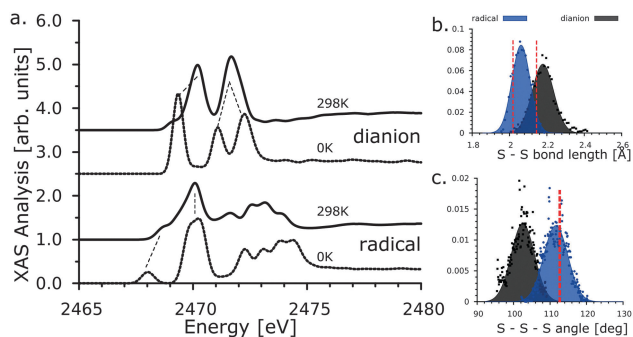
Fig. 6 (a) Comparison the calculated S K-edge XAS of trisulfur radical ($S_3^{•-}$) and dianion (S_3^{2-}) species from the optimized geometry at 0 K (dashed line) and sampled from an AIMD simulation at 298 K (solid line). The thin dashed lines indicate the correspondence between the peaks at 0 K and 298 K (b) distribution of the S–S bond length of the radical (blue) and dianion (black) species during 298 K AIMD simulation. The data (points) are fit to a Gaussian (lines) for presentation purposes. The equilibrium S–S bond lengths at 0 K are indicated by the vertical dashed red lines. (c) Distribution of the S–S–S bond angle during 298 K AIMD simulation.

these atoms (Fig. 5). There is a corresponding 1s → π^* transition for the internal sulfur atom, which our calculations indicate is blue shifted by 2.2 eV compared to the terminal atoms. The red shift of XAS peak positions of the terminal atoms, relative to internal atoms, reflects the accumulation of electron density around the terminal atoms, which provides more valence electronic screening to reduce the core-electron binding energies of these atoms, generating a significant core-level shift. In fact, the increased charge density around the terminal sulfur atoms is so significant that the higher energy 1s → σ^* transitions become coincident with the 1s → π^* transition of the internal sulfur atom, and constitutes the broad feature in the XAS between 2470 and 2471 eV. The higher energy XAS features, beyond 2472 eV, results from two sets of spin dependent 1s → σ^* transitions of the internal sulfur atom. These sets of σ^* states are split by

~2.1 eV, where the lower energy state (denoted a1*) has electron density in the core-excited state that is not aligned with either S–S bond (i.e. a non-bonding state), while the higher energy state (b2*) is a more traditional anti-bonding σ^* with electron density along the S–S bond. Similar to disulfur, the XAS at 298 K is generally red-shifted, smoother and much broader than at 0 K. For example, the previously distinct low energy π^* peak in the radical XAS at 0 K merges with the low energy σ^* peak and presents as a shoulder near 2468.7 eV. Analysis of our AIMD trajectory reveals that these spectral changes results from a 10% increase in the S–S bond lengths and 1% decrease in the S–S–S bond angle compared to the equilibrium structure at 0 K.
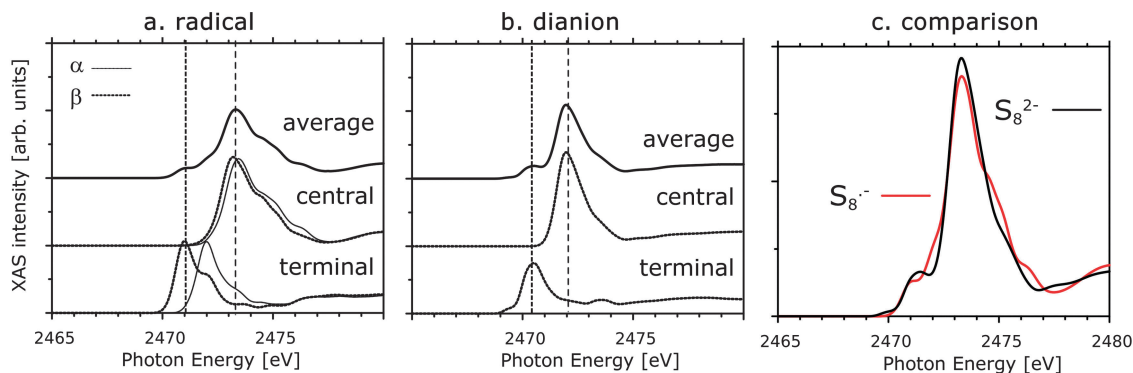
Turning now to the S_3^{2-} trisulfur dianion at 0 K, we find that the XAS is characterized by three main features: (1) a broad, low energy shoulder near 2469.4 eV that arises from excitations to the terminal sulfur atoms (2) a major peak near 2470.9 eV that arises from the terminal sulfur atom and (3) a second major peak near 2473.0 eV again arising from the central sulfur atom. At 298 K, the intensity of the 1st major peak is reduced and split into two features: a minor, low energy peak near 2469.1 eV and a major peak near 2670.3 eV. This reflects sampling displacements along the asymmetric and symmetric stretching modes in the molecule. By the same token, the higher energy σ^* peaks that are distinct and separated at 0 K merge at 298 K and present as a single feature centered near 2673.1 eV (Fig. 6).

2.3. Longer chain linear polysulfides

In Fig. 7a we compare the XAS of a radical and dianionic tetrasulfur molecule. Generally, the XAS is characterized by a pre-edge feature near 2470.3 eV, which arises primarily from the two terminal atoms and a main edge feature near 2472.5 eV, which arises primarily from the two central sulfur atoms. In the radical, the lowest energy transition is a down spin (minority channel) 1s → π^* transition, yet unlike the distinct peak in trisulfur, this peak is much closer to the low energy 1s → σ^*
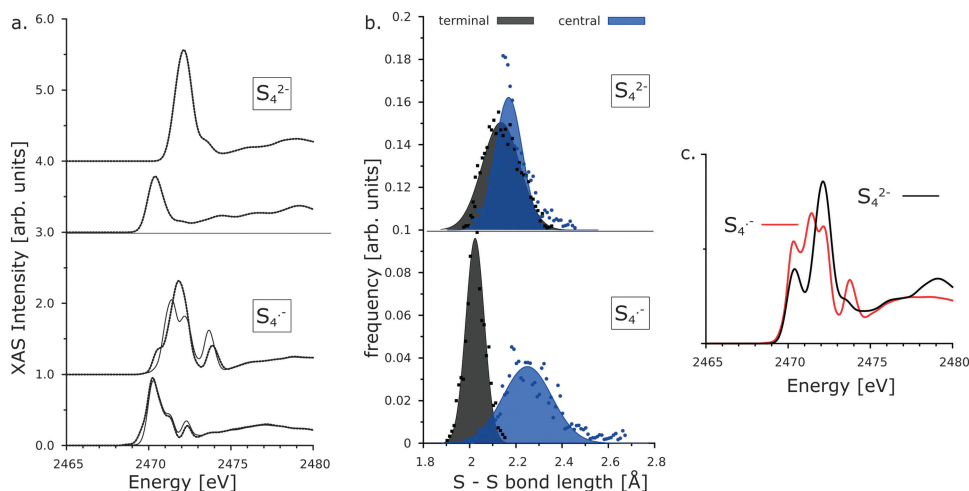
Fig. 7 (a) Calculated S K-edge XAS of the tetrasulfur radical $S_4^{•-}$ and dianion S_4^{2-} ion. The total XAS spectra is separated into contributions arising from the terminal and central atoms, and from the majority (dotted line) and minority (dashed line) spin channels. (b) Distribution of the S–S bond length during AIMD simulations for the radical (top panel) and dianion (bottom panel). We separately analyze the S–S bond distributions of central (blue filled curve) and terminal (black curve) atoms. (c) Comparison of the calculated S K-edge XAS of the radical $S_4^{•-}$ and dianion S_4^{2-} tetrasulfur ions.

7748 | Phys. Chem. Chem. Phys., 2015, 17, 7743–7753

This journal is © the Owner Societies 2015

Fig. 8 From left to right: calculated S K-edge XAS of octasulfur molecules: the (a) radical $S_8^{\bullet-}$; (b) dianion S_8^{2-}; and (c) a comparison between the two. The total XAS is decomposed into contributions arising from only the two terminal and two central S atoms. Additionally, the XAS of the radical ion is separated into contributions arising from the majority and minority spin channels.

peaks and presents a faint should near 2469.2 eV. We also find that the main-edge peak is split into two features, one centered near 2471.9 eV and another centered near 2473.1 eV, and is a signature of asymmetric bonding around the internal sulfur atoms: analysis of the S–S bond distribution indicates a bimodal distribution, where the internal S–S bond is longer than the terminal bonds by ∼0.2 Å. On the other hand, analysis of the S–S bonds in the dianion indicates that the central S–S bond is only 0.05 Å longer than the terminal bonds. In this case, the central S atoms experience a much more symmetric bonding environment and the corresponding XAS peak is not visibly split.

Considering an even longer chain polysulfide, we find that the differences in the XAS of the radical and dianionic species is further reduced for the linear (broken chain) octasulfur (Fig. 8). Similar to tetrasulfur, the XAS of both species are generally characterized by a pre-edge feature near 2470.9 eV, arising from transitions to the unoccupied energy levels of the two terminal sulfur atoms, and the main-edge feature near 2472.9 eV, arising from the six central atoms. Delocalization of the excess atomic charge and a broad S–S bond distribution in the S_8 chains result in smooth XAS features. In particular, we find that the low energy π^* feature of the radical, although present, is no longer visible in the XAS, but rather merges with the low energy σ^* features and contributes sparingly to the intensity of the pre-edge feature.

3. Discussion

3.1. The origin of the pre-edge peak in the XAS

So far, we have predicted that the pre-edge features in the S K-edge XAS of linear polysulfides (radicals or dianions) arise primarily from the terminal sulfur atoms and are not exclusively due to radical species. We now present a thought experiment to support this hypothesis. Consider an isolated, cyclic S_8 molecule (no broken bonds). We created a radical variant of this molecule (cyclo $S_8^{\bullet-}$) by adding an additional electron to the system and relaxing the geometry isotropically. This radical, cyclic $S_8^{\bullet-}$ molecule is interesting, since it might be the initial species in the discharge process at the cathode of Li–S electrochemical cells.
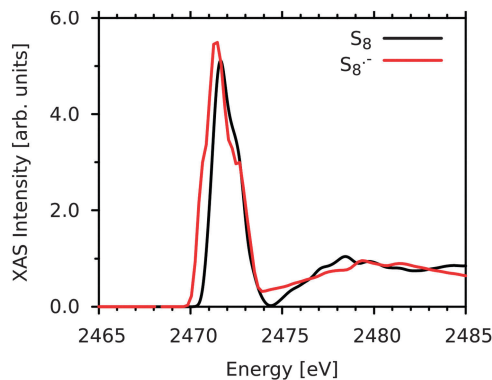

Fig. 9 Comparison of the calculated S K-edge XAS of a neutral and radical S_8 molecule.

At the DFT-PBE level, our optimization leads to a slightly larger molecule, with an average increase in the S–S bonds of 0.2 Å. As shown in Fig. 9, the XAS of the radical and neutral S_8 molecules are virtually indistinguishable, with the only appreciable difference being a 0.1 eV red shift in the XAS of the radical, reflective of the additional screening and longer S–S bonds. Further, since the SOMO of the radical is of the same σ^* character as the LUMO of the neutral molecule, the low energy π^* feature, that is a signature of the linear radical polysulfides, is no longer present in the XAS. This example reaffirms that the presence of dangling (i.e., terminal) S–S bonds, and not charge state, is predominantly responsible for the pre-edge feature in linear polysulfides. The one exception is the trisulfur radical, where the 1s → π^* transition in the internal sulfur atom accounts for ∼30% of the intensity of the pre-edge feature.

3.2. The effect of solvent environment

From our analysis of the finite temperature distributions of bond lengths and angle of the gas phase linear polysulfides, we have shown how structural fluctuations give rise to generally broader spectra, with red-shifts induced by thermal expansion. We find that not only are the peak positions affected by finite temperature distortions, the intensity of the features at 298 K are significantly different than at 0 K. In previous work we considered
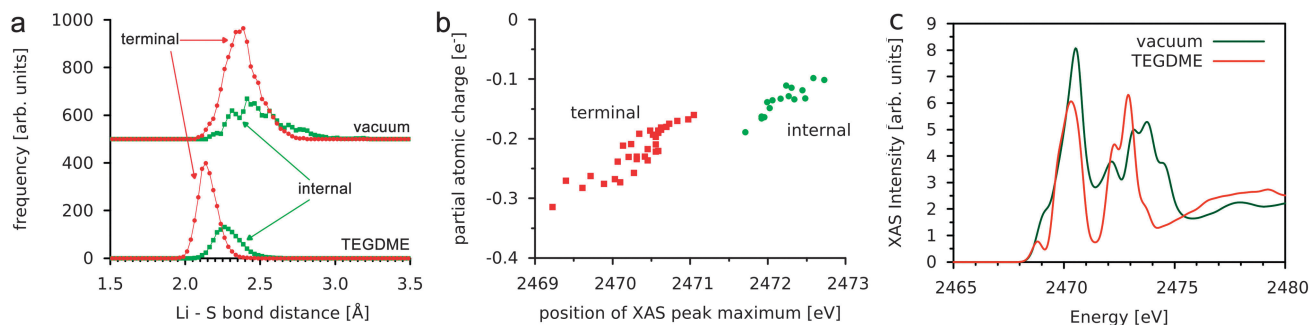
Fig. 10 (a) Comparison of the lithium−sulfur coordination (radial distribution function) of LiS$_3$ in tetraglyme (TEGDME – top panel) and vacuum (bottom panel). Li–S distances to the terminal (red circles) and internal (green squares) atoms is obtained from 298 K AIMD simulations. (b) Correlation between the positions of the XAS peak maximum and the partial atomic charges of S atoms of LiS$_3$ in vacuum from a 298 K AIMD simulation. We separately consider the XAS of the internal (green) and terminal (red) atoms. (c) Comparison of the calculated XAS of LiS$_3$ in vacuum (green) and dissolved in TEGDME (red).

a range of polysulfide dianions dissolved in tetraglyme (tetra-ethylene glycol dimethyl ether, TEGDME).[21] The peak positions from our current calculations, sampling gas phase configurations, are red-shifted by ∼0.75 eV compared to those of a trisulfur dianion dissolved in tetraglyme. Given these differences, one could reasonably doubt whether XAS spectra obtained from sampling gas phase AIMD simulations are representative of a typical experimental context, where polysulfides are usually dissolved in solvent.

In order to address this issue, we calculated the XAS of a LiS$_3$ radical molecule dissolved in tetraglyme by sampling an AIMD trajectory. At finite temperature, the LiS$_3$ complex exhibits far greater structural fluctuations in gas phase than in the solvent. In particular, as demonstrated by the width of the Li–S distribution profiles (Fig. 10a), the lithium ion is much more mobile in the vacuum, leading to larger charge fluctuations and longer S–S bonds. Since the position of the peak maximum is linear correlated with the partial atomic charge on the excited atom (Fig. 10b), the red shift of the peak positions in solution is due to this effect. Additionally, due to the less fluxional structure in the solvent, the XAS of LiS$_3$ dissolved in tetraglyme at room temperature more closely resembles the XAS at 0 K (rather than 298 K) in the gas-phase.

3.3. The XAS signature of radical polysulfides

Finally, we return to the low energy π* feature in the XAS of the radical polysulfide molecules. As noted above, this feature is unique to radicals, and could be used to identify them even in polysulfide mixtures, since X-ray transitions to the filled π* orbitals of dianions are not possible. In the trisulfur radical, we predict that the π* peak would appear as a distinct feature between 2468 and 2469 eV, although with low intensity. We note that XAS measurements on samples that contain the trisulfur radical trapped in Lazurite mineral[26] contains a broad peak between 2467 and 2469 eV. Analysis of this data revealed that this peak could in fact be a convolution of two separate features, one centered near 2469 eV and another, weaker feature centered near 2467.5 eV. In light of our calculated results, and considering the additional screening of the unoccupied states dues to the aluminosilicate cage which would red-shift

the peak positions, it is reasonable to propose that the low energy feature is the 1s → π* peak of the terminal trisulfur radical ion.

The low intensity of the π* feature is due to a core-excited state with little electron density around the excited (terminal) atoms. This stands in contrast to the increased electron density around the excited atom in core-excited states of σ* symmetry. We rationalize the shift in electron density away from the core-excited terminal atoms as follows: (1) the ground state SOMO is a delocalized, anti-bonding state with π* symmetry; (2) generating a core-hole on a terminal atom shifts its local atomic orbitals down in energy and actually increases the local electron density at that site; (3) the π* SOMO, an antibonding orbital, now shifts its probability density away from the electron-enriched terminal core-excited atom, whose atomic orbitals are drawn significantly out of resonance with the other two S atoms; (4) hence, the lowest energy orbital accessible to the core-excited electron is the empty (minority-spin) version of this asymmetric π* SOMO. On the other hand, the core-excited internal sulfur atom acts instead to redistribute electron density more evenly across the S$_3$ molecule, which supports a more symmetric probability distribution for the core-excited π* electron density, leading to a more intense absorption feature albeit at a higher energy.

The relatively low intensity of the radical-specific terminal-atom π* feature should make XAS detection difficult. Indeed, our calculations indicate that this feature would only be appreciable for a S$_3^{•−}$ radical mole fraction (relative to other dianionic polysulfides) >20% (Fig. 11). The absence of this low-energy feature in any polysulfide measurements to date, and, in particular, for samples purported to contain such high concentrations of radicals,[24] suggests a reinterpretation of the experimental measurements and reassessment of the proposed electrochemical pathways is required. If radicals are present at all in significant amounts in polysulfide mixtures (at rest or at finite bias) then perhaps complimentary X-ray spectroscopies might reveal them. Our prediction of a low-energy π* feature, below the typical pre-edge, suggests that resonant X-ray emission spectroscopy (RXES),[42] may be more appropriate for radical detection. RXES records emission spectra as a function of incoming X-ray photon energy.
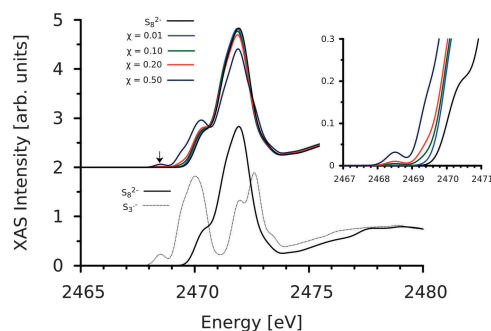
7750 | Phys. Chem. Chem. Phys., 2015, 17, 7743–7753

This journal is © the Owner Societies 2015

Fig. 11 (Bottom panel) comparison of the calculated S K-edge XAS of the trisulfur radical (dotted line) and a linear lithium octasulfur (Li$_2$S$_8$: solid line) both dissolved in TEGDME. (Top panel) composite XAS of an increasing mole fraction of LiS$_3$ (χ) relative to Li$_2$S$_8$. The black downward arrow indicates the position of the low energy 1s $\rightarrow$ π^* feature of the terminal atoms (inset) zoom of XAS between 2467 and 2471 eV showing the various LiS$_3$ mole fractions.

By restricting the incoming X-ray energy to 2468–2469 eV, the 1s $\rightarrow$ π^* transitions of the trisulfur radical can be exclusively probed and emission spectra characteristic of the radical alone should be detected.

4. Conclusions

The reaction chemistries that facilitate the charging–discharging of Li–S batteries are as yet unknown and may indeed involve radical polysulfide species as intermediates. There remains a clear need for probes that can identify these species in solution. Based on the spectra of trapped radicals in Lazurite mineral cages, a pre-edge feature at $\sim$2470 eV in sulfur K-edge X-ray absorption has been purported as evidence of these radical species. Our DFT-XCH XAS calculations of the XAS of polysulfides indicate, however, that pre-edge features arise primarily from sulfur atoms at the ends of linear polysulfides, irrespective of charge state. Specifically, for the trisulfur radical, we find an additional lower energy feature near 2468 eV that arises from its half-filled π^* orbital, which is absent in the dianion, since this orbital is filled. This π^* peak should be a distinctive feature of the trisulfur radical as it appears below the aforementioned 2470 eV pre-edge, however its intensity is rather weak and we predict that it may not be visible in experimental XAS of polysulfide mixtures for radical mole fractions <20%. We have seen no evidence for such an absorption feature in polysulfide measurements to date, which indicates that sulfur radical species are not present in large mole fractions.

5. Computational methods

5.1. Structure optimization

As stated, all density functional theory calculations employ the Perdew–Burke–Ernzerhof[35] generalized-gradient approximation to the exchange–correlation functional. We optimized each starting structure by placing the molecule in a cubic cell (length 2 nm) and performing conjugate-gradient minimization of the total energy

with respect to the atomic positions using the PWSCF code within the Quantum-Espresso package.[43] Our plane-wave pseudopotential calculations used ultrasoft pseudopotentials and a kinetic energy cut-off for electronic wave functions (density) of 25 (200) Ry.

5.2. *Ab initio* molecular dynamics simulations

The PBE-DFT optimized structures were used as input to an AIMD simulation using a modified version of the mixed Gaussian and plane wave code[44] CP2K/Quickstep.[45] We employed a triple-ζ basis set with two additional sets of polarization functions (TZV2P)[46] and a 320 Ry plane-wave cutoff. The same PBE functional is employed,[35] and the Brillouin zone is sampled at the Γ-point only. Interactions between the valence electrons and the ionic cores are described by norm-conserving pseudopotentials.[47,48] Solutions to the Poisson equation are provided by an efficient Wavelet-based solver.[49] We overcome the poor description of the long-range dispersive forces within the PBE-GGA exchange–correlation functional by employing the DFTD3 empirical corrections of Grimme *et al.*[50] For each system, we performed at least 50 ps of constant volume constant temperature (*NVT*) dynamics, saving a snapshot of the system (atomic coordinates and velocities) at every step. The temperature of the system was kept near 300 K using a Nose–Hoover thermostat (temperature damping constant of 100 fs). We allowed for 20 ps of equilibration and 100 snapshots for the system from 20–50 ps (evenly spaced every 30 fs) as input to our DFT-XCH X-ray absorption calculations.

5.3. Spin polarized DFT-XCH XAS calculations

X-ray absorption spectra were calculated within a spin-polarized generalization of the eXcited electron and Core Hole Density Functional Theory (XCH-DFT) approach.[40] Within the traditional XCH approach, the lowest energy core-excited state is modeled explicitly using a self-consistent DFT framework, taking into account the effects of the core-hole (*via* an appropriate pseudo-potential) and the screening from the excited electron. The self-consistent core-excited Hamiltonian describing this lowest excited reference state is then diagonalized and the energies of higher-lying X-ray excited states relative to the reference state are inferred from Kohn–Sham eigenvalue differences in the resulting eigenspectrum.

In the absence of an absolute energy reference for excited states, due to the use of pseudopotentials which remove explicit core-electrons, we make use of a previously devised approach which references excited states to a theoretical isolated atom.[51,52] Accordingly, the energy of the lowest X-ray transition E_T for a given core-level on a specific atom of element A within the chemical system of interest is given by

$$E_T = (E_{XCH} - E_{GS}) - (E_{XCH}^A - E_{GS}^A) - \varepsilon_{XCH}^{SOMO} + \Delta \quad (1)$$

where E_{XCH} is the self-consistent XCH total energy of the supercell modeling the core-excited system; E_{GS} is the total energy of the same supercell with the system in its ground state; E_{XCH}^A, E_{GS}^A are XCH and ground state total energies of an isolated atom of type A respectively; ε_{XCH}^{SOMO} is the Kohn–Sham eigenvalue of the molecular orbital singly occupied by the excited electron

in the XCH solution and Δ is a constant shift (the same for all atoms of a given element: +2467.2 eV for sulfur) that is determined based on alignment to a single experimental reference (the first main peak of gaseous SF_6[53]). Within a spin-polarized version of this scheme, we separately model the lowest energy X-ray transition in the two (α and β) spin-channels by simulating self-consistently the promotion of a core-electron of a given spin into the lowest available empty valence orbital of the same spin. The core-hole is modeled using a pseudopotential as usual. Since the spin of the core-electron is not explicitly taken into account this leads to two different values of the total spin projection of the valence electrons in the XCH final state for the two cases. The energy of the lowest X-ray transition E_T^σ in spin-channel σ for a given core-level on a specific atom of element A within the chemical system of interest is given by

$$E_T^\sigma = (E_{XCH}^\sigma - E_{GS}) - (E_{XCH}^A) - \varepsilon_{XCH}^{HOMO,\sigma} + \Delta$$

where E_{XCH}^σ is the self-consistent XCH total energy of the supercell modeling the core-excited system with the excited electron in spin-channel σ, $\varepsilon_{XCH}^{HOMO,\sigma}$ is the Kohn–Sham eigenvalue of the highest occupied molecular orbital with spin σ in the XCH final state, while the rest of the quantities have the same meaning as in eqn (1). For the excited electron in a given spin-channel, the spin-polarized XCH Hamiltonian is diagonalized and Kohn–Sham eigenvalues having the same spin index are used to infer the energies of higher-lying X-ray transitions within this spin-channel. Furthermore, Kohn–Sham wavefunctions corresponding to the same spin-channel are used to calculate dipole transition matrix elements. This is done separately for both α and β spins and the spin-resolved spectra are added to obtain the total spectrum.

All our XCH calculations employed the same periodic boundary conditions as our AIMD simulations, and used the PBE-GGA functional,[35] and plane-wave pseudopotentials with a kinetic energy cut-off for the electronic wave functions (density) of 25 (200) Ry. Core-excited ultrasoft pseudopotentials and corresponding atomic orbitals were generated with the Vanderbilt code.[54] Matrix elements representing transition amplitude of the core-excited excitations were evaluated within the projector-augmented-wave (PAW) frozen-core approximation.[55] The PWSCF code within the Quantum-ESPRESSO package[43] was used to generate the core excited Kohn–Sham eigenspectrum, while the Shirley interpolation scheme[56] was used to accelerate numerical convergence of the computed spectra. The calculated XAS is taken as the statistical average of the spectrum of every sulfur atom in the structure, which includes intrinsic line shape broadening resulting from finite temperature effects at 298 K, but we also include a 0.2 eV Gaussian convolution to guarantee a continuous spectral contribution from each atom.

Acknowledgements

References

1 K. W. Mlynarski, US Geological Survey, 2000.

2 N. N. Greenwood and A. Earnshaw, *Chemistry of the elements*, Pergamon Press, Oxford [Oxfordshire], New York, 1984.

3 A. Vairavamurthy, *Spectrochim. Acta, Part A*, 1998, **54**, 2009–2017.

4 B. Meyer, *Chem. Rev.*, 1976, **76**, 367–388.

5 N. N. E. A. Greenwood, *Chemistry of the elements*, Pergamon Press, Oxford [Oxfordshire], New York, 1984.

6 D. Peramunage and S. Licht, *Science*, 1993, **261**, 1029–1032.

7 A. Manthiram, Y. Fu and Y.-S. Su, *Acc. Chem. Res.*, 2012, **46**, 1125–1134.

8 S. Evers and L. F. Nazar, *Acc. Chem. Res.*, 2012, **46**, 1135–1143.

9 S. E. Cheon, S. S. Choi, J. S. Han, Y. S. Choi, B. H. Jung and H. S. Lim, *J. Electrochem. Soc.*, 2004, **151**, A2067–A2073.

10 R. D. Rauh, F. S. Shuker, J. M. Marston and S. B. Brummer, *J. Inorg. Nucl. Chem.*, 1977, **39**, 1761–1766.

11 L. Nazar, M. Cuisinier, P.-E. Cabelguen, B. Adams, A. Garsuch and M. Balasubramanian, *Energy Environ. Sci.*, 2014, **7**, 2697–2705.

12 C. Barchasz, F. Molton, C. Duboc, J.-C. Leprêtre, S. Patoux and F. Alloin, *Anal. Chem.*, 2012, **84**, 3973–3980.

13 M. U. Patel, R. Demir-Cakan, M. Morcrette, J. M. Tarascon, M. Gaberscek and R. Dominko, *ChemSusChem*, 2013, **6**, 1177–1181.

14 H. Wang, Y. Yang, Y. Liang, J. T. Robinson, Y. Li, A. Jackson, Y. Cui and H. Dai, *Nano Lett.*, 2011, **11**, 2644–2647.

15 M. Cuisinier, P.-E. Cabelguen, S. Evers, G. He, M. Kolbeck, A. Garsuch, T. Bolin, M. Balasubramanian and L. F. Nazar, *J. Phys. Chem. Lett.*, 2013, **4**, 3227–3232.

16 J. Gao, M. A. Lowe, Y. Kiya and H. D. Abruna, *J. Phys. Chem. C*, 2011, **115**, 25132–25137.

17 J. Nelson, S. Misra, Y. Yang, A. Jackson, Y. Liu, H. Wang, H. Dai, J. C. Andrews, Y. Cui and M. F. Toney, *J. Am. Chem. Soc.*, 2012, **134**, 6337–6343.

7752 | *Phys. Chem. Chem. Phys.*, 2015, **17**, 7743–7753

This journal is © the Owner Societies 2015

18 M. U. M. Patel, I. Arčon, G. Aquilanti, L. Stievano, G. Mali and R. Dominko, *ChemPhysChem*, 2014, **15**, 894–904.

19 L. Ji, M. Rao, H. Zheng, L. Zhang, Y. Li, W. Duan, J. Guo, E. J. Cairns and Y. Zhang, *J. Am. Chem. Soc.*, 2011, **133**, 18522–18525.

20 M. Vijayakumar, N. Govind, E. Walter, S. D. Burton, A. Shukla, A. Devaraj, J. Xiao, J. Liu, C. Wang and A. Karim, *Phys. Chem. Chem. Phys.*, 2014, **16**, 10923–10932.

21 T. A. Pascal, K. H. Wujcik, J. J. Velasco-Velez, C.-H. Wu, A. A. Teran, M. Kapilashrami, J. Cabana, J. Guo, M. Salmeron and N. P. Balsara, *J. Phys. Chem. Lett.*, 2014, **5**, 1547–1551.

22 A. Prange, I. Arzberger, C. Engemann, H. Modrow, O. Schumann, H. G. Truper, R. Steudel, C. Dahl and J. Hormes, *Biochim. Biophys. Acta, Gen. Subj.*, 1999, **1428**, 446–454.

23 J. M. Durand, J. OlivierFourcade, J. C. Jumas, M. Womes, C. M. Teodorescu, A. Elafif, J. M. Esteva and R. C. Karnatak, *J. Phys. B: At. Mol. Phys.*, 1996, **29**, 5773–5784.

24 M. A. Lowe, J. Gao and H. D. Abruña, *RSC Adv.*, 2014, **4**, 18347–18353.

25 K. H. Wujcik, J. Velasco-Velez, C. H. Wu, T. Pascal, A. A. Teran, M. A. Marcus, J. Cabana, J. Guo, D. Prendergast and M. Salmeron, *J. Electrochem. Soc.*, 2014, **161**, A1100–A1106.

26 M. E. Fleet and X. Liu, *Spectrochim. Acta, Part B*, 2010, **65**, 75–79.

27 R. J. Clark and D. G. Cobbold, *Inorg. Chem.*, 1978, **17**, 3169–3174.

28 T. Chivers and I. Drummond, *Inorg. Chem.*, 1972, **11**, 2525–2527.

29 F. Seel, H.-J. Guttler, G. Simon and A. Wieckowski, *Pure Appl. Chem.*, 1977, **49**, 45–54.

30 V. L. Tauson, J. Goettlicher, A. N. Sapozhnikov, S. Mangold and E. E. Lustenberg, *Eur. J. Mineral.*, 2012, **24**, 133–152.

31 S. Tarling, P. Barnes and J. Klinowski, *Acta Crystallogr., Sect. B: Struct. Sci.*, 1988, **44**, 128–135.

32 V. Martin-Diaconescu and P. Kennepohl, *J. Am. Chem. Soc.*, 2007, **129**, 3034–3035.

33 S.-I. Tobishima, H. Yamamoto and M. Matsuda, *Electrochim. Acta*, 1997, **42**, 1019–1029.

34 T. Chivers and P. J. Elder, *Chem. Soc. Rev.*, 2013, **42**, 5996–6005.

35 J. P. Perdew, K. Burke and M. Ernzerhof, *Phys. Rev. Lett.*, 1996, **77**, 3865–3868.

36 J. Tossell, *Geochim. Cosmochim. Acta*, 2012, **95**, 79–92.

37 T. Fueno and R. J. Buenker, *Theor. Chim. Acta*, 1988, **73**, 123–134.

38 G. Herzberg, *Molecular spectra and molecular structure. Vol. 1: Spectra of diatomic molecules*, Van Nostrand Reinhold, New York, 2nd edn, 1950, p. 1.

39 E. Rühl, R. Flesch, W. Tappe, D. Novikov and N. Kosugi, *J. Chem. Phys.*, 2002, **116**, 3316–3322.

40 D. Prendergast and G. Galli, *Phys. Rev. Lett.*, 2006, **96**, 215502.

41 M. E. Fleet, X. Liu, S. L. Harmer and H. W. Nesbitt, *Can. Mineral.*, 2005, **43**, 1589–1603.

42 B. K. Agarwal, *Springer Ser. Opt. Sci.*, 1979, **15**, 35–46.

43 P. Giannozzi, S. Baroni, N. Bonini, M. Calandra, R. Car, C. Cavazzoni, D. Ceresoli, G. L. Chiarotti, M. Cococcioni and I. Dabo, *J. Phys.: Condens. Matter*, 2009, **21**, 395502.

44 G. Lippert, J. Hutter and M. Parrinello, *Mol. Phys.*, 1997, **92**, 477–487.

45 J. VandeVondele, M. Krack, F. Mohamed, M. Parrinello, T. Chassaing and J. Hutter, *Comput. Phys. Commun.*, 2005, **167**, 103–128.

46 J. VandeVondele and J. Hutter, *J. Chem. Phys.*, 2007, **127**, 114105.

47 S. Goedecker, M. Teter and J. Hutter, *Phys. Rev. B: Condens. Matter Mater. Phys.*, 1996, **54**, 1703–1710.

48 M. Krack, *Theor. Chem. Acc.*, 2005, **114**, 145–152.

49 L. Genovese, T. Deutsch and S. Goedecker, *J. Chem. Phys.*, 2007, **127**, 054704.

50 S. Grimme, J. Antony, S. Ehrlich and H. Krieg, *J. Chem. Phys.*, 2010, **132**, 154104.

51 A. H. England, A. M. Duffin, C. P. Schwartz, J. S. Uejio, D. Prendergast and R. J. Saykally, *Chem. Phys. Lett.*, 2011, **514**, 187–195.

52 P. Jiang, D. Prendergast, F. Borondics, S. Porsgaard, L. Giovanetti, E. Pach, J. Newberg, H. Bluhm, F. Besenbacher and M. Salmeron, *J. Chem. Phys.*, 2013, **138**, 024704.

53 R. E. LaVilla and R. D. Deslattes, *J. Chem. Phys.*, 1966, **44**, 4399–4400.

54 D. Vanderbilt, *Phys. Rev. B: Condens. Matter Mater. Phys.*, 1990, **41**, 7892–7895.

55 G. Kresse and D. Joubert, *Phys. Rev. B: Condens. Matter Mater. Phys.*, 1999, **59**, 1758.

56 E. L. Shirley, *Phys. Rev. B: Condens. Matter Mater. Phys.*, 1996, **54**, 16464.

57 M. Cuisinier, C. Hart, M. Balasubramanian, A. Garsuch and L. F. Nazar, *Adv. Energy Mater.*, 2015, DOI: 10.1002/aenm.201401801.

58 G. Henkelman, A. Arnaldsson and H. Jónsson, *Comput. Mater. Sci.*, 2006, **36**, 354–360.

59 R. F. Bader, *Atoms in molecules*, Wiley Online Library, 1990.

This journal is © the Owner Societies 2015

Phys. Chem. Chem. Phys., 2015, **17**, 7743–7753 | 7753